2021

Harvesting Heat from Safer, Energy-Dense Slow Pyrolant Mixtures for Future Space Missions

Katerina Chagoya
University of Central Florida

HARVESTING HEAT FROM SAFER, ENERGY-DENSE SLOW PYROLANT MIXTURES FOR FUTURE SPACE MISSIONS

by

KATERINA CHAGOYA
B.S. University of Central Florida, 2016

A thesis submitted in partial fulfillment of the requirements
for the degree of Master of Science
in the Department of Mechanical and Aerospace Engineering
in the College of Engineering and Computer Science
at the University of Central Florida
Orlando, Florida

Summer Term
2021

Major Professors: Jayanta S. Kapat and Richard G. Blair

ABSTRACT

Energy sources powering space missions range from highly energetic nuclear reactions to short-lifetime and low-output batteries. The proper selection of a power system is dependent on the mission duration and destination and oftentimes energy sources that may be optimal for the former may be unsuitable for the latter. Various limitations of these power sources hinder the capacity for regular and frequent space exploration. However, the ability to harvest heat for electrical power generation would allow for long-distance and long-duration missions at a reduced cost. By employing a regulated, self-propagating, exothermic chemical reaction between solid fuel and oxidizer, we hope to devise a slow-burning reactant system capable of generating heat at a harvestable rate. Eighteen energy-dense fuel and oxidizer combinations were selected to assess for their slow-propagating potential. One ceramic and one graphite propagation cell were designed to monitor combustion along a linear length of pyrolant powder and to measure reaction temperatures. Each reaction was ignited through heating of a nichrome wire placed at one end of the pyrolant mixture and four thermocouples were placed at 1 cm intervals along the length of powder following the wire. In addition to the propagation cell, a multi-step selection process was devised to evaluate each pyrolant. By this process, the pyrolant mixture between lithium peroxide and boron was selected, and the best propagation rate achieved by this system was measured to be 1.49 cm/s.

This is dedicated to Benji,

who loved it when I wrote papers or did homework,

because that meant I would be staying at home with him for a very long time

and he wouldn't need to wait by the door or scratch at it

if I was out doing anything else.

ACKNOWLEDGMENTS

I would like to acknowledge my research advisor, Dr. Richard Blair, for his guidance in my undergraduate and graduate studies and throughout this project. I would also like to acknowledge Dr. Jayanta Kapat and Dr. Subith Vasu for their assistance in various ways as I proceeded through the mechanical engineering program.

For financial support, I thank the National Aeronautics and Space Administration (NASA) for funding as part of the NASA ESI 2019 grant.

Thank you to my coworkers and fellow students that have been a source of positivity for me through this journey, especially Fernand Torres-Davila, our adopted group member and the best unofficial labmate. Thanks for always “needing to use the glovebox” so I have someone to run experiments with, and for the best coquito every Christmas. I would like to thank the many undergraduate students who have assisted me in research throughout the years, especially Emma Blanco, who made thermocouple welding much more bearable for this project in particular, as well as both Jose Berger and Elan Marrero for their jokes, the bad and the good, respectively.

Thank you to my closest friends and family, including Deepti Siddhanti, for the laughs, the outings, and all the support during my undergraduate days through to now and also to Lavina Ranjan for the emotional and familial support, no matter how far away on Earth you both are. Thank you to Wesley Blevins for being a great listener and friend, and for growing up with me and not without me. A special thank you to David Nash, who helps me with everything and more, I wouldn’t be getting a Masters degree without you. Thank you to my parents, Teodozja and Rudy Chagoya, for constantly asking me how much longer until I finish school, and to my brother and sis Demetri and Michelle Chagoya, for kindly not pestering me with such questions.

TABLE OF CONTENTS

LIST OF FIGURES

LIST OF TABLES

CHAPTER 1: INTRODUCTION AND MOTIVATION

1.1 Human Space Exploration

Since the start of human space exploration in the late 1950s, the number of space programs and agencies across the globe have grown, humans have sent probes and spacecraft to distant parts of the solar system, and humans themselves have left the planet. It can be said that the past 65 years of space travel and discovery have provided humanity with some of the greatest technological and scientific advancements of any other age[1]. However, it can also be said that space exploration is not occurring fast enough, since high impact missions are launched typically on the order of years or decades. Political[2, 3], legal[4-6], and societal[7] challenges and constraints are commonly debated as potential explanations for humanity's slow space colonization progress. However, construction of a spacecraft and its components are non-trivial and complex, not to mention the physical human limitations[8-10] which are now in the spotlight as conversations turn to increased manned missions and long-term outer space habitability.

Currently, the United States' National Aeronatics and Space Administration (NASA) is the most active and funded space organization on Earth [11]. A mission to space within NASA's Planetary Missions Program will fall into one of three groups: Discovery, New Frontiers, or Solar System Exploration (Table 1)[12]. Small missions which require few resources and short development times fall into the Discovery class, which can potentially launch a spacecraft from Earth in as little as 36 months (3 years) of the mission's conception. These Discovery class missions define today's standards for "frequent" human space exploration. However, our most ambitious and compelling missions do not have such short development times, nor do they have comparable budgets. Missions involving high-priority science objectives that strive to investigate a range of questions commonly fall under Solar System Exploration [12]. These are the flagship

missions (now called Large Strategic Science Missions) for the Planetary Science division, and their costs enter the range of billions of dollars[12].

Table 1: NASA's Planetary Missions Program classifies missions into 3 groups. [12]

Program	Mission Budget	Development Time	Class	Description
Discovery	$450 million	36 months	Small missions	➢ Established in 1992 ➢ Missions require fewer resources ➢ Selection process: peer-reviewed competition
New Frontiers	$850 million	60 months	Mid-size	➢ Established in 2003 ➢ Missions bridge gap between flagship and Discovery class ➢ Selection procees: peer-reviewed competition ➢ High-priority Planetary Science Community mission goals
Solar System Exploration	$2 – 3 billion	>5 years	Flagship	➢ High priority targets ➢ Often missions of national importance ➢ Selection Process: None. Missions assigned directly to a NASA center

This high cost and lengthy development time comes in part from the scientific instruments on board, as well as the power system for the craft. Flagship missions typically require robust materials and complex equipment in order to accomplish the ambitious goals of the mission. Although decreasing the costs associated with each analytical instrument onboard a spacecraft is a wide and complicated task, devising low-cost power sources is not outside our reach. A low-cost and versitile mode of energy production could drop some high-priority missions down from Flagship class to a lower class, allowing for more frequent launches to these high-priority targets and shortening the timeline of scientific discovery.

1.1.1 Spacecraft Power Systems

Space agencies are continually searching for innovative power solutions which would enable more flexibility when planning missions [13-17]. Energy sources powering space missions

can range from highly energetic nuclear reactors to short-lifetime and low-output batteries (Figure 1) [18]. Batteries are conventional and convenient, but require recharging if they are to be used over the course of weeks or months. In addition, batteries may not contain sufficient outputs to power all the instruments that may be desired on board, leaving scientists to prioritize some scientific equipment over others. This is now another constraint in addition to weight restrictions. Novel technologies such as regenerative fuel cells are a promising source of energy that could further diversify fuel options [18, 19]. For the Artemis program, NASA plans to widen the scope of their sustainable power generation through public prize competitions such as the Watts on the Moon Challenge[20], launched in 2021, which intends to solve the problem of powering sustained living on the Moon.

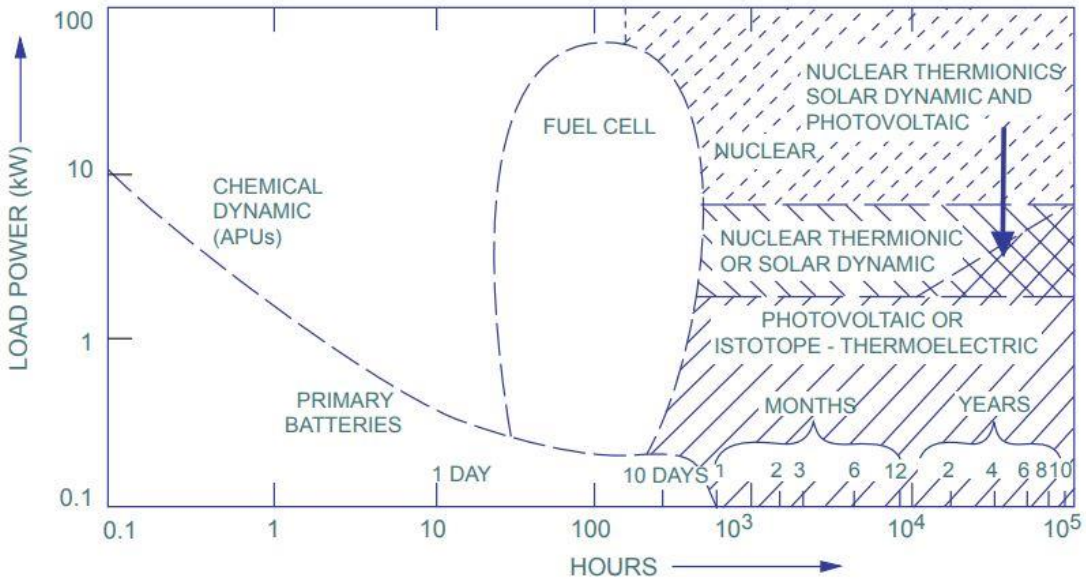

Figure 1: The range of power output and lifetimes of various energy sources for spacecraft. [18]

The proper selection of a power system is dependent on a multitude of variables, including the mission duration and the destination. Oftentimes, an energy source that has an appropriate

lifetime for a mission may not be a suitable choice for the destination, or vice-versa. For example, solar arrays paired with lithium-ion batteries may operate well on missions as far as Mars, but this power quickly diminishes with increasing distance [21]. To date, only the Juno spacecraft, launched in 2011 to Jupiter, has successfully utilized solar panels to generate power at a distance greater than Mars (Figure 2) [21]. However, Lucy, JUICE, and the Europa Clipper will soon travel to the Trojan asteroids, Jupiter, and Europa while utilizing large-area solar arrays to fuel their batteries. For the Europa Clipper, these solar arrays will span about 100 feet in order to receive sufficient sunlight [22]. Moreover, even some missions to the Moon and Mars may require alternatives to solar power in order to overcome specific challenges, such as cold temperatures at high altitudes, at the poles, or during winter season, as well as sunless locations [23]. Likewise, manned missions to any destination will require power other than solar [24].

Figure 2: An illustration of NASA's Juno spacecraft, exhibiting its large solar arrays.

1.1.2 Radioisotope Thermoelectric Generators (RTGs)

Radioisotope thermoelectric generators (RTGs) have powered several long-range, long-duration, and energy-intensive space missions, most of which are listed in Table 2. Pioneer 10-11, Voyager 1-2, Galileo, Cassini, New Horizons (Figure 3), and Dragonfly have destinations to the Jovian planets and beyond, which are too large of a distance from the sun for solar panels to operate efficiently. The Ulysses spacecraft, whose mission was to collect data from the Sun's poles, required a gravity-assist maneuver around Jupiter in order to escape the plane of the Solar System [25]. The detour to Jupiter ruled out the possibility of a solar-powered mission to study the Sun.

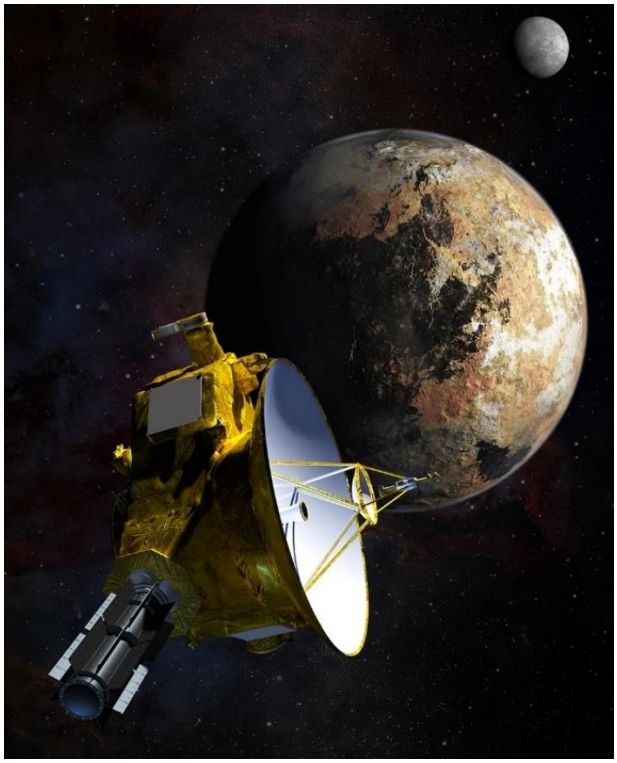

Figure 3: An illustration of New Horizons, an example of a spacecraft powered by an RTG.

RTGs provide a thermal fuel source that also maintains ideal equipment operating temperatures onboard the craft. Their simple operation and low maintanence requirements make them suitable for unmanned missions to the most extreme environments in space and on Earth.

RTGs operate continuously and independent of certain unavoidable circumstances such as variations in sunlight, temperature, dust, and radiation [24].

Table 2: List of spacecraft powered by a radioisotope thermoelectric generator.

Spacecraft	Mission Destination	Launch Year	Years Active	RTG Type	Isotope	Class
Apollo 12 – 17	Moon	1969-72		SNAP-27	Pu-238	N/A
Pioneer 10	Jupiter	1972	31	SNAP-19	Pu-238	N/A
Pioneer 11	Jupiter/Saturn	1973	22	SNAP-19	Pu-238	N/A
Viking Landers 1, 2	Mars	1975		mod. SNAP-19	Pu-238	Flagship
Voyager 1, 2	Interstellar Space	1977	43	MHW-RTG	Pu-238	Flagship
Galileo	Jupiter	1989	14	GPHS-RTG	Pu-238	Flagship
Ulysses	Sun	1990	19	GPHS-RTG	Pu-238	N/A
Cassini	Saturn	1997	20	GPHS-RTG	Pu-238	Flagship
New Horizons	Pluto/Kuiper Belt	2006	15	GPHS-RTG	Pu-238	New Frontiers
Curiosity Rover	Mars	2011	10	MMRTG	Pu-238	Flagship
Perserverance Rover	Mars	2020	1	MMRTG	Pu-238	Flagship
Dragonfly	Saturn	2026	0	MMRTG	Pu-238	New Frontiers

An RTG can be fueled by a number of isotopes, including americium-241 and strontium-90, which is commonly used at remote locations on Earth. Plutonium-238 is NASA's isotope of choice for spacecraft, and it is provided in the form of plutonium dioxide pellets ($^{238}PuO_2$). Radioisotopes offer power options on the order of tens of kilowatts, which is lower than some chemical fuels and most nuclear power options. However, their lifetimes are far greater, in the range of years, as illustrated in Figure 4. Although the power output capabilities of an isotope degrade over time based on its half-life, Pu-238 retains most of its heat output within half a decade of its creation.

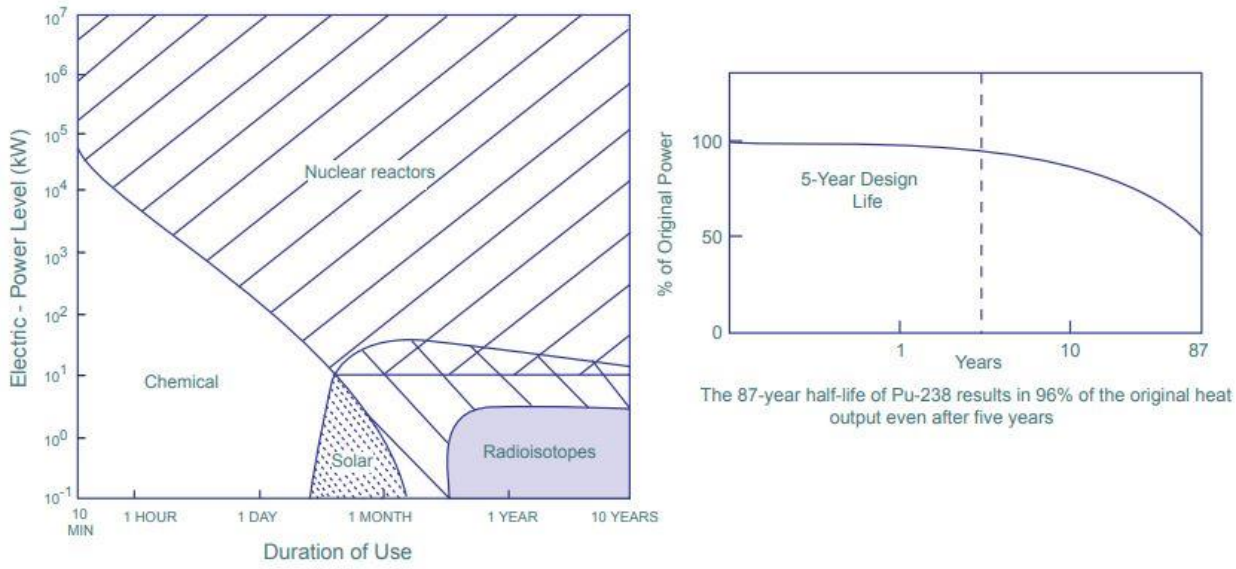

Figure 4: (Left) Lifetime and power output of a radioisotope thermoelectric generator. (Right) The remaining power able to be produced by the RTG accounting for isotope decay.

Over time, there have been several generations of RTG technology to meet the power needs of their spacecrafts. The Systems for Nuclear Auxillary Power (SNAP), one of the first variations, had an initial power output of approximately 40 and 70 W for the SNAP-19 and SNAP-27, respectively. The Multi-Hundred Watt (MHW-RTG) power source employed on Voyager 1 and 2 more than doubled the output of the SNAP-27, at 158 watts of power at the mission start. The general purpose heat source RTG (GPHS-RTG) is a combination of 18 GPHS modules which provided a total power output of 292 W at the beginning of the Galileo, Ulysses, Cassini, and New Horizons missions. Galileo and Cassini both utilized more than one GPHS-RTGs (2 and 3 for Galileo and Cassini, respectively) [26]. The newest generation, named the multi-misson radioisotope thermoelectric generator (MMRTG) was designed to operate not only in the vaccum of space, but also within a planetary atmosphere. The MMRTG (Figure 5) was first utilized on the Curiosity Rover as part of the Mars Science Laboratory mission launched in 2011 and contains 8 GPHS modules, collectively generating about 110 W of power.

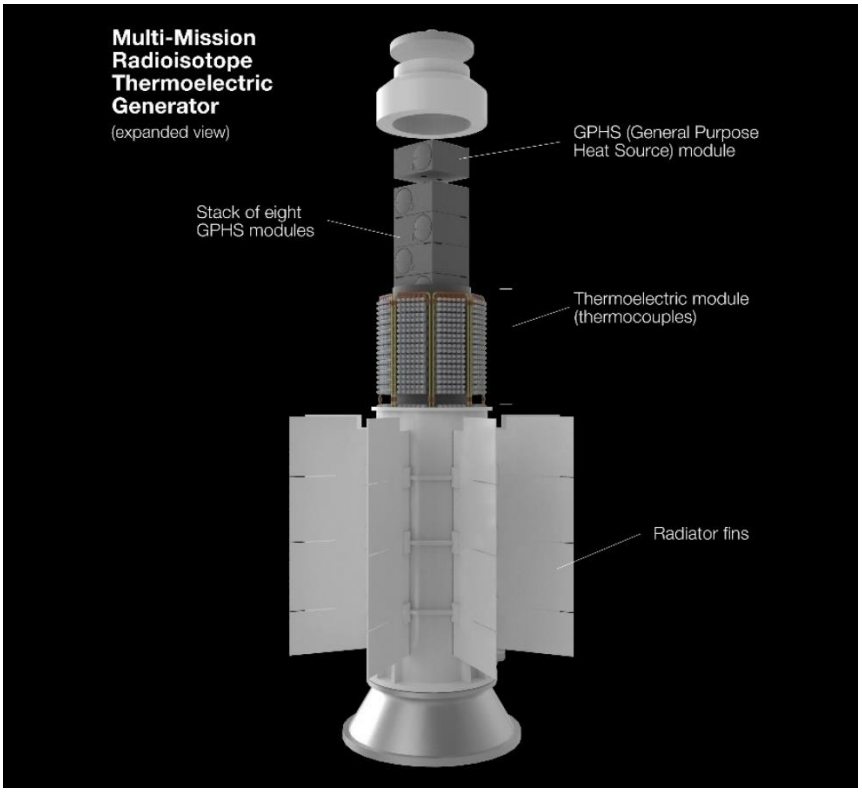

Figure 5: A multi-mission radioisotope thermoelectric generator (MMRTG) consisting of 8 GPHS modules, and thermocouples which convert the generated heat into electricity.

As much as the RTG has fascilitated the most ambitious of NASA's flagship missions, there are grounds for diversifying spacecraft power options. The United States halted it's production of plutonium in 1988, making new plutonium-238 difficult to source . The plutonium already in the U.S. stockpile could only provide fuel for 3 additional MMRTGs, one of which currently powers the Perseverence Rover which landed on Mars in 2021, and another which is reserved for the future Dragonfly mission to Titan. Although Oak Ridge National Laboratory has since began producing Pu-238 again in small quantities under the US Department of Energy Supply Project, the goal is to produce 1.5 kg/year by 2026 [27]. A single MMRTG requires approximately 3.4 kg of Pu-238, whereas the GPHS-RTG requires 7.7 kg [24].

If NASA is to increase the frequency of its flagship missions, attempts to unrestrict itself from the RTG should be made. The capability of generating a steady flow of heat for a long period of time need not be dominated exclusively by radioisotopes. Solid-state exothermic reactions could potentially provide the necessary heat for electrical power generation, which would provide a similar enclosed, environmentally-resistant power source, allowing for long-distance and long-duration missons at a reduced cost.

1.2 Solid State Exothermic Reactions

The heat produced by solid-state exothermic reactions could potentially be harvested as energy to power missions that would otherwise be powered by an RTG. The exothermic condition is met by any chemical reaction which contains a negative value for enthalpy, which can be calculated using Equation 1.1 for a typical chemical reaction [28].

$$\Delta H^{\circ} = \sum H_{products} - \sum H_{reactants} \tag{1.1}$$

The more negative a value of enthalpy, the more heat produced by a reaction, whereas an overall positive enthalpy value indicates an endothermic reaction, or one which requires heat input. A thorough explantation of the enthalpy calculation for a balanced chemical reaction is provided in the section to follow. We seek to determine chemical reactions with the most negative enthalpies for potential use as slow burning pyrolants. The enthalpy value for a chemical reaction system can then be utilized to quantify the maximum temperature reached by the burning reactants in a closed system, which is the subject of the next section.

1.2.1 Calculating Adiabatic Temperature

It is important to determine the maximum temperature capable of our exothermic reactions

in order to assess which reaction should provide the largest quantity of heat able to be harvested. Such a temperature is termed the adiabatic temperature (T_{ad}) and this quantity differs from a reaction's enthalpy. Although an exothermic chemical reaction may produce heat upon completion, not all of this energy is released as heat or is usable for work. The energy produced from reagents can be absorbed by the products in different vibrational modes (the products' heat capacities) as well as in phase changes, if such an event occurs. Therefore, the value obtained from an enthalpy calculation might indicate a larger production of heat than is usable in reality, and can be seen as a theoretical value until heat capacity and other heat sinks specific to a chemical reaction have been accounted for.

The concept employed for this calculation involves initially quantifying the total enthalpy of the reaction. This is accomplished using the chemical reaction containing all starting reagents, and with the general knowledge of the most likely product(s) to be formed. Given a chemical reaction between reagents A and B which produce the products C and D, the stoichiometric coefficients (a, b, c, and d, respectively) must be found by balancing the chemical equation, which should result in something resembling Equation 1.2. The overall reaction enthalpy can then be calculated using Equation 1.3 (which is an expanded version of Equation 1.1), if the enthalpies of formation (H_f) are known for each reagent and product at STP (standard temperature and pressure) [28]. The degree sign included in the abbreviation for enthalpy, $\Delta H°$, refers to the standard enthalpy of formation when the reagents are at STP. Typically, enthalpies of formation for specific compounds can be found at STP in reference texts, literature, or chemical databases such as the National Institute of Standards and Technology (NIST) Chemistry WebBook Database [29].

$$aA + bB \rightarrow cC + dD \tag{1.2}$$

$$\Delta H^{\circ} = \left(cH_{f,C} + dH_{f,D}\right) - \left(aH_{f,A} + bH_{f,B}\right) \tag{1.3}$$

Once the specific enthalpy ($\Delta H°$) has been obtained, we can begin the process of determining T_{ad}. The following paragraphs will first describe the logic behind the calculation, followed by a handful of formulas needed before we can perform the T_{ad} calculation, and will end with putting the pieces together to obtain T_{ad}.

We must begin with the assumption that products C and D were formed with 100% yield (the reaction went to completion and reagents A and B are no longer present). With a system now containing only products, a series of accounting steps can be taken at small increments of temperature beginning at 298 K (room temperature). For each incremental rise in temperature, ΔT, of products C and D, we will determine the heat (Q) that must have been absorbed by these compounds to increase their temperature, and we will subtract that heat, Q, from the total standard enthalpy, $\Delta H°$. In addition, if one of the products should undergo a phase change at a specific temperature, the heat required for that phase change is subtracted from the total enthalpy, $\Delta H°$, until all the energy produced by the exothermic reaction has been expended (i.e. $\Delta H°=0$). At the point when the internal energy, $\Delta H°$, has been expended, whatever temperature the products C and D have reached is the adiabatic temperature.

Of course, in reality, the chemistry of a reaction is unlikely to proceed in this way. It is unlikely that 100% of the product is formed at room temperature at which point the products begin to absorb the produced exotherm. It is more plausible that the consuption of reagents to produce products, heat production, heat absorption, and phase changes occur together and at times simultaneously. However, accounting for the order of these events can be impossible as well as unnecessary for bookkeeping the released heat.

Here will be given a general example of the adiabatic temperature calculation for a generic chemical reaction which may look like Equation 1.2. We will discuss a few different heat sinks,

or phenomena which would cause the products to absorb heat. However, we will assume adiabatic conditions, meaning we will assume no heat travels outside the system of our compounds to the environment. The heat sinks we will consider are listed in Table 3.

Table 3: Types of heat sinks to consider for adiabatic temperature calculations.

Heat Sink	Quantity Needed	Abbrev.	Unit
Heat absorbtion: storage in molecular vibrational modes	Heat capacity (const. pressure) as a function of temp	$C_p(T)$	J/molK
Phase change: melting	Heat of fusion	ΔH_{fus}	kJ/mol
Phase change: Evaporation	Heat of vaporization	ΔH_{vap}	kJ/mol

Some amount of the heat produced by the chemical reaction will be absorbed by the reaction products C and D, each of which can store the kinetic energy in the form of molecular vibrations. Depending on the bonds contained by the compounds C and D, the heat can be stored in a bond stretching, bending, or twisting, which together we will call the heat capacity, C_p, of that compound or molecule. Heat capacities for different compounds can be found at STP in reference texts and chemical databases. However, to increase accuracy it is best to determine the heat capacity as a function of temperature, $C_p(T)$, which can be found using the Shomate equation (Equation 1.4), where constants L, M, N, O, and P are determined experimentally and for many compounds are often listed in the NIST Chemistry WebBook Database [29]. In Equation 1.4, t is a fraction of temperature described by Equation 1.5.

$$C_p^\circ = L + Mt + Nt^2 + Ot^3 + Pt^{-2} \tag{1.4}$$

$$t = {}^{T}/_{1000} \ (T \ in \ Kelvin) \tag{1.5}$$

For a chemical reaction containing a single product C, calculating the Shomate equation one time to determine $C_p(T)$ for only compound C completes the work required for this step. However, for chemical reactions containing multiple products C + D (or even C + D + E), an

average heat capacity must be calculated based on the mass fractions of C and D produced. Since different molecules contain different bond types, each molecule C, D, or E will contain a different value for heat capacity and each need to be considered. The equation for calculating average heat capacity is shown in Equation 1.6, where X_C and X_D are the mass fractions of compounds C and D, respectively. The calculations for obtaining the mass fractions are shown in Equations 1.7 and 1.8, where m indicates the compound's respective masses. Due to the conservation of mass, Equation 1.9 must be true. In addition, the sum of the fractions of all products must equal unity (Equation 1.10). The procedure for determining the final product masses m_C and m_D can be calculated from chemical Equation 1.2 if the molecular weights and stoichiometric coefficients (a, b, c, and d) are known. A detailed explanation of this calculation can be found in any general chemistry textbook.

$$C_{p,avg} = C_{p,C}X_C + C_{p,D}X_D \tag{1.6}$$

$$X_C = \frac{m_C}{m_C + m_D} \tag{1.7}$$

$$X_D = \frac{m_D}{m_C + m_D} \tag{1.8}$$

$$m_{total} = m_A + m_B = m_C + m_D \tag{1.9}$$

$$X_C + X_D = 1 \tag{1.10}$$

Of course, the result of Equation 1.6 ($C_{p,avg}$) is not a measure of heat itself, and cannot be subtracted from $\Delta H°$ directly since they are not both measures of energy. The quantity of heat, Q, absorbed by the products in order to increase the temperature by ΔT is dictated by Equation 1.11.

$$Q_{\Delta T} = m_{total} C_{p,avg} \Delta T \tag{1.11}$$

Refering back to Table 3, heat can also be absorbed by the compounds C and D in the event of a phase change, in which the energy will be stored in the general movements of the molecules. The heat of fusion of a compound, C, is the amount of energy *input* required for C to undergo a phase change from a solid to a liquid (melting). Moreover, the heat of fusion can also indicate the amount of energy *released* by C if it were to undergo solidification from a liquid to a solid. For a compound C, this value should be equivalent (but opposite sign) in either direction (melting or solidifying). Similarly, the heat of vaporization of a compound, C, is the amount of energy *input* required for C to undergo a phase change from vaporization of liquid to a gas, or energy *released* in the event of condensation of C from gas to liquid. To calculate the heat absorbed by such a phase change, Equations 1.12 and 1.13 can be used. Q_{melt} or Q_{vap} can also be referred to as the latent heat [28].

$$Q_{melt,C} = \frac{m_C}{MW_C} \Delta H_{fus,C} \tag{1.12}$$

$$Q_{vap,C} = \frac{m_C}{MW_C} \Delta H_{vap,C} \tag{1.13}$$

During any of these 4 types of phase changes, the overall temperature, T, of the products should not change; all the energy should temporarily be directed exclusively to changing the physical state of the compounds and no change in temperature should occur. The heat of fusion or vaporization of a compound can be found in reference texts or chemical databases. The temperature at which these occur are, of course, specific to the melting point and boiling point of the particular compound.

Combining all of these steps, we are finally able to quantify the adiabatic temperature. It may be convenient to use a spreadsheet or other software to calculate each step in ΔT, since it is ideal to use small increments in temperature which may significantly increase the number of calculations necessary. In a generic example in Table 4 below, I will use increments of 10 K, as shown in the first column. The first column defines the temperature of the products. Using this temperature, we can calculate $C_{p,avg}$ for column 2. Then, using the average heat capacity the various Qs in column 3 can be quantified. All that follows is continually subtracting this determined heat quantity, Q, from the ΔH° "bank account" until the ΔH° reaches zero (and the bank account is empty). The temperature at which the total internal energy ΔH is depleted, is the adiabatic temperature. It is key to know the melting and boiling points of all products in order to determine the point at which a switch must be made from calculating Q from heat absorbtion to calculating Q_{melt} or Q_{vap}.

Table 4: Example of adiabatic temperature calculation using a spreadsheet. Notice the last calculation should occur when the total enthalpy reaches zero.

$T_{products}$ (K)	**$C_{p,avg}$ for C + D**	**Energy Requirement**	**ΔH remaining**	**Heat sink type**
T_1	$C_{p,avg\ @T1}$	$Q_1 = m_{products}*C_{p,avg\ @T1}*(T_2-T_1)$	$\Delta H_1 = \Delta H° - Q_1$	Heat absorbtion
$T_2 = T_1 + 10K$	$C_{p,avg\ @T2}$	$Q_2 = m_{products}*C_{p,avg\ @T2}*(T_3-T_2)$	$\Delta H_2 = \Delta H_1 - Q_2$	Heat absorbtion
$T_3 = T_2 + 10K$	$C_{p,avg\ @T3}$	$Q_3 = m_{products}*C_{p,avg\ @T3}*(T_4-T_3)$	$\Delta H_3 = \Delta H_2 - Q_3$	Heat absorbtion
…	…	…	…	…
$T_x = T_{mp,\ C}$		$Q_{melt} = \Delta H_{fus,C}*m_C/MW_C$	$\Delta H_x = \Delta H_{x-1} - Q_{melt}$	Phase change: melting
…	…	…	…	…
$T_y = T_{mp,\ D}$		$Q_{melt} = \Delta H_{fus,D}*m_D/MW_D$	$\Delta H_y = \Delta H_{y-1} - Q_{melt}$	Phase change: melting
…	…	…	…	…
$T_n = T_{ad}$	$C_{p,avg\ @Tn}$	$Q_n = m_{products}*C_{p,avg\ @Tn}*(T_n-T_{n-1})$	0	Heat absorbtion

If the values for C_p or ΔH_f cannot be found, they can be estimated by looking to similar chemical compounds for reference. Heat capacities are quantities based on the amount of heat stored in a molecule's bonds as they rotate or vibrate. Thus, a molecule containing similar bonds can be used as an analog. It is important to consider ionic vs covalent bonds, as well as intermolecular bonds. Heats of formation can depend on the initial phase of the compound as well as its crystal structure if in the solid phase.

CHAPTER 2: RESEARCH OBJECTIVES

2.1 Solid State Exothermic Reactions as an Energy Source

The central research objective of this study was to find a candidate solid-state exothermic reaction to use as an energy source and determine its propagation speed. The energy densities of several fuel and oxidizer combinations were calculated, and a list of 18 were chosen for preliminary experimentation (Table 5). The chemical compounds chosen were required to be in the solid phase and were expected to be generally pyrolitic. However, it was critical that at least one reaction could maintain a steady burn rate, rather than expend itself rapidly and all at once. A steady burn rate implies long-duration heat generation if properly managed as well as the possibly for controlled burning. Thus, the ideal pyrolant candidate is one whose propagation rate is naturally slow, and which does not require additives or other heat sinks to slow its propagation to a desirable rate. Although this is the desirable behavior, methods can be employed for pyrolants with rapid burn rates in an attempt to slow them down.

Table 5: List of 18 fuel and oxidizer reaction combinations to test for slow reaction propagation potential.

#	Fuel	Oxidizer	Energy Density (kWh/kg)	#	Fuel	Oxidizer	Energy Density (kWh/kg)
Group 1: Lithium Peroxide				**10**	Al	MnO_2	1.35
1	B	Li_2O_2	2.09	**11**	Al	MoO_3	1.31
2	MgB_2	Li_2O_2	2.83	**Group 3: Magnesium & Teflon**			
3	Mg	Li_2O_2	2.28	**12**	Mg	Fe_2O_3	1.29
4	TiB_2	Li_2O_2	1.68	**13**	Mg	Fe_3O_4	1.2
5	Si (nano)	Li_2O_2	2.83	**14**	Mg	CuO	1.28
6	Zr	Li_2O_2	1.48	**15**	Mg	MnO_2	1.54
Group 2				**16**	Mg + Si	O_2	8.57
7	Ti	B	1.54	**17**	Mg	$(C_2F_4)_n$	4.1
8	Ti	C	0.85	**18**	Li	$(C_2F_4)_n$	3.4
9	Si (nano)	O_2	9.04				

In order to measure burn propagation rates, a test cell was designed to monitor combustion along a length of reaction powder. Prior to any analysis within the propagation test cell, a series of

experimental tests were devised to evaluate each of the 18 exothermic reactions. These preliminary evaluations shortened the experimental process considerably, rapidly eliminating reactions that were violently exothermic and avoided breakage of the test cell. For this selection process, reactions were organized into groups roughly according to their chemical compositions in order to distinguish ignition patterns.

CHAPTER 3: EXPERIMENTAL METHODS

3.1 Production of Solid Pyrolant Mixtures

Stoichiometric quantities of solid fuel and oxidizer were measured on an analytical balance. The powders were homogeneously mixed by hand-shaking in a glass serum vial, followed by grinding in a mortar and pestle, and then finally loading into an empty steel vial to be shaken for 15 minutes by a mixer mill. The resulting powders are shown in Figure 6.

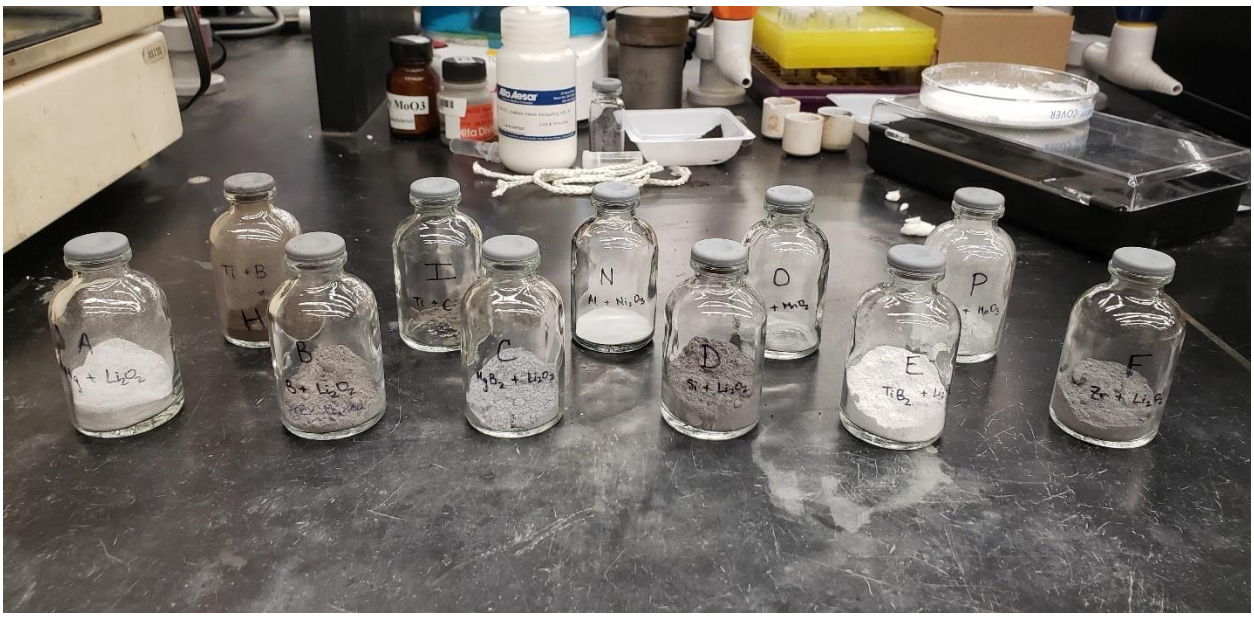

Figure 6: A view of a select number of the 18 pyrolant powders, after homogenizing the fuel and oxidizer.

3.2 Selection of the Ideal Pyrolant Candidate

A selection process was devised to determine the best pyrolant candidates and to narrow down to a suitable number for initial testing. The pyrolants were subjected to 3 preliminary experimental tests: a) a wire ignition and explosivity test, b) thermogravimetric analysis (TGA) and c) a vertical propagation test. Each test was designed to assess one or multiple variables to select the pyrolant candidate that would require the least amount of manipulation or chemical additives to propagate slowly.

3.2.1 Wire Ignition and Explosivity Test

At the outset, pyrolants were analyzed for their ability to be ignited with a nichrome wire, as this is ultimately the ignition device within the propagation reaction chamber. Simultaneously, their physical explosivity was assessed. A coil of nichrome wire was placed at the bottom of a small, open, ceramic crucible (Figure 7). Approximately 0.5 g of pyrolant was placed on top and around the coil, covering it completely. The nichrome wire was heated for 5 seconds by generating a current within it in order to ignite the pyrolant powder.

Figure 7: A post-combustion image of burned solid pyrolant in a ceramic crucible, atop a coiled nichrome wire. The reaction product has hardened around the wire coil.

3.2.2 Thermogravimetric Analysis (TGA)

Pyrolants which passed the ignition and explosivity test proceeded to be analyzed through thermogravimetric analysis (TGA). Pure fuel and oxidizer powders were also analyzed. The instrument contained an alumina pan attached to a platinum hang wire (Figure 8). The samples were heated to 600 °C at a rate of 10 °C/min under a flow of air. The moisture content of the powders, evolution of gases, and ignition temperatures were determined by monitoring mass fluctuations in the powders.

Figure 8: Thermogravimetric analysis (TGA) was used to monitor mass fluctuations of the pyrolants during ignition. The right image shows a sample of titanium and boron pyrolant mixture hanging on the weighing pan.

3.2.3 Vertical Propagation Test

Pyrolants which passed the ignition and explosivity test proceeded to a vertical propagation test rig, shown in Figure 9. This rig consists of a cylindrical chamber with removable bottom and top covers, all constructed of POCO graphite. A small channel was machined from the top through the bottom down the long axis of the cylinder, excluding the lid and base (Figure 9a). This chamber contains the pyrolant powder during combustion. Four thermocouples penetrate the side of the cylinder (Figure 9c) and enter the central channel, embedding themselves in the center of the pyrolant powder. The thermocouple holes are spaced 1 cm apart. At the bottom of the cylinder, a hollow alumina tube is inserted horizontally, which holds the nichrome ignition wire (Figure 9b). The alumina tube acts as insulation to shield the ignition wire from the graphite surroundings, which are highly electrically conductive, and can interfere with wire heating. A hole is cut in the alumina tube where it will lie under the narrow channel so the pyrolant powder makes contact with the ignition wire (Figure 9d), but does not fall through the bottom of the graphite cylinder.

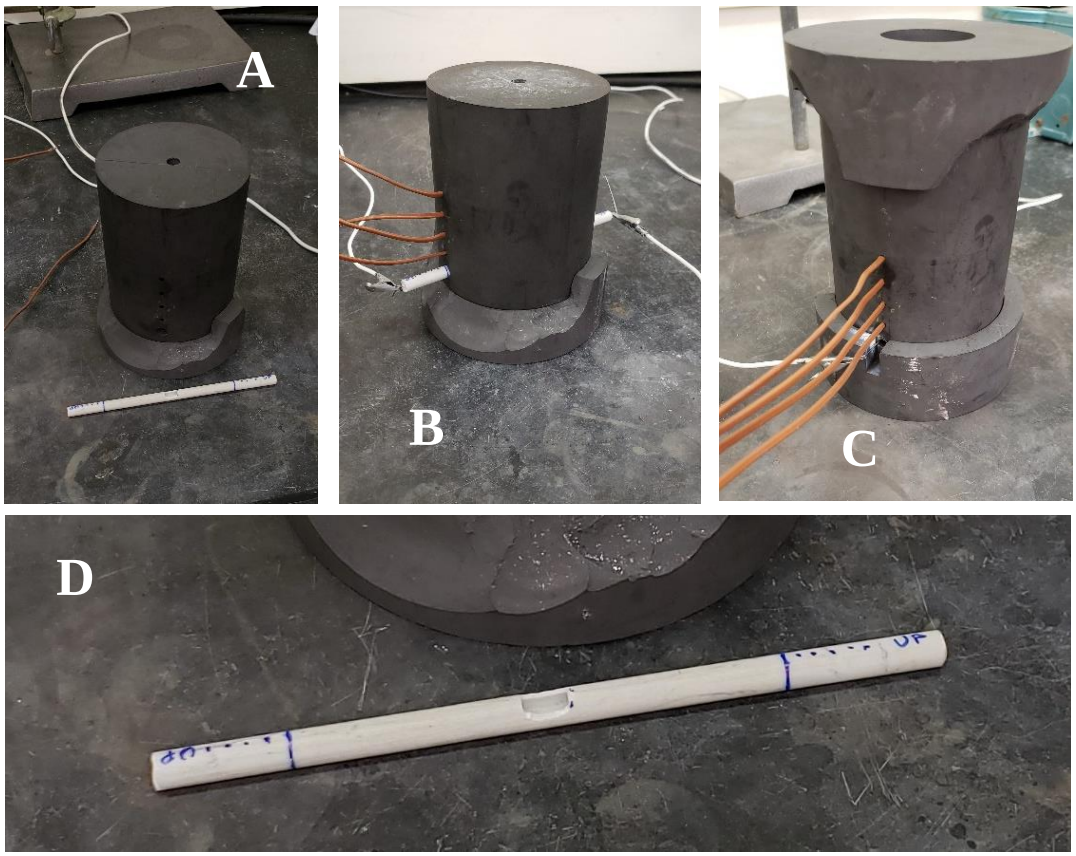

Figure 9: (A) The vertical graphite test chamber, showing the top opening of the channel which holds the pyrolant. (B) A hollow alumina tube hods the ignition wire and is inserted horizontally through the bottom of the graphite cylinder. (C) 4 thermocouples are inserted into the side of the cylinder and reach the interior of the channel where they make contact with the pyrolant. (D) A close-up of the alumina tube, showing a cut hole designed to align with the pyrolant channel.

Thus, the pyrolant placed in this vertical propagation cell ignites from the bottom of the cylinder and propagates upwards. The nichrome wire is heated for 7 seconds to ignite the pyrolant. Pyrolant was packed into the central chamber until it reached 1 cm above the topmost thermocouple.

3.3 Thermocouple Coatings

Observations of noise in the temperature readings during pyrolant burning resulted in various attempts to coat thermocouples using different compounds.

Polysilizane was applied to 4 bare, welded thermocouple wires using a cotton applicator, shown in Figure 10a. The liquid was applied heavily and dried in an oven at 180 °C to harden.

A mixture of boron nitride and isopropanol was spray-coated onto 4 bare, welded thermocouple wires using a spray coater attached to compressed air (Figure 10b). These thermocouples were left to air dry.

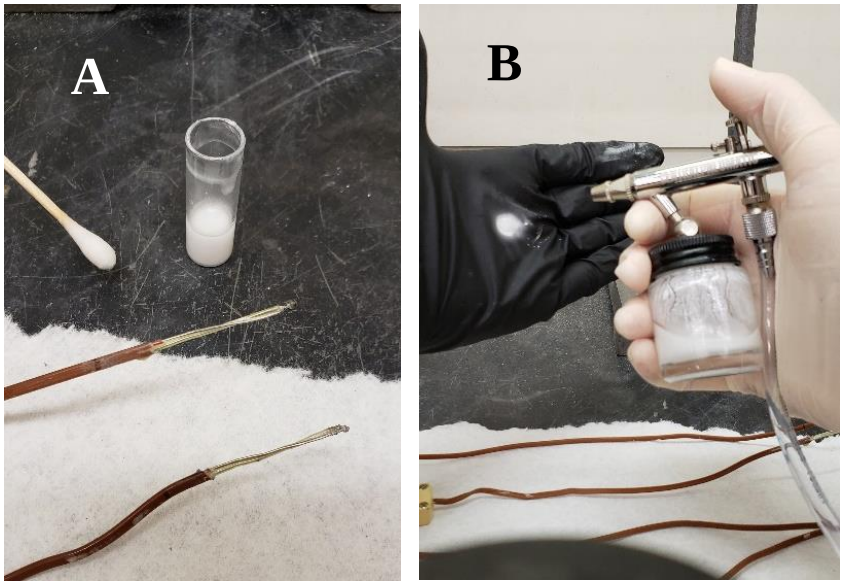

Figure 10: (A) Stripped thermocouples were coated with polysilizane applied with cotton applicator. (B) Stripped thermocouples were coated with a mixture of boron nitride powder in isopropyl alcohol using a spray coater.

3.4 Measuring Reaction Propagation

Propagation rates were evaluated for each pyrolant reaction within specially constructed propagation test cells. Two nearly identical cells were machined: one of ceramic and the other of graphite (Figures 11 and 12). Each cell consists of 4 ceramic or graphite blocks which are cut such that when assembled, they create an empty rectangular space between them. A stainless steel base and lid, as well as bolts, hold the 4 blocks in place.

For each experiment, approximately 1 g of pyrolant mixture is loaded into the rectangular chamber space, which when completely closed compresses the powder gently to form a rectangle,

as shown in Figure 11c. A nichrome wire at one end of the rectangular chamber is coiled where it is imbedded in the pyrolant, and the wire ends extend out each side of the cell to be connected to a variable AC transformer (Variac); this placement is shown in Figure 11b. As the powder is ignited from one side to the other, thermocouples inserted at 1 cm intervals along the length of the sample measure the heat generated. Ten channels are machined perpendicular to the sample chamber (Figure 11d) which hold the thermocouples at precise intervals from each other and ensure they do not shift during burning. Only 4 of these channels are used at a time, but additional channels allow for changing the thermocouple placement along the pyrolant sample if desired. Each reaction is ignited by heating the nichrome wire for 7 seconds. The equal spacing between the 4 thermocouples allows for a rate calculation as the combustion front passes over each thermocouple. Figure 11d shows the pyrolant chamber after a successful ignition of pyrolant that began looking as that of Figure 11c.

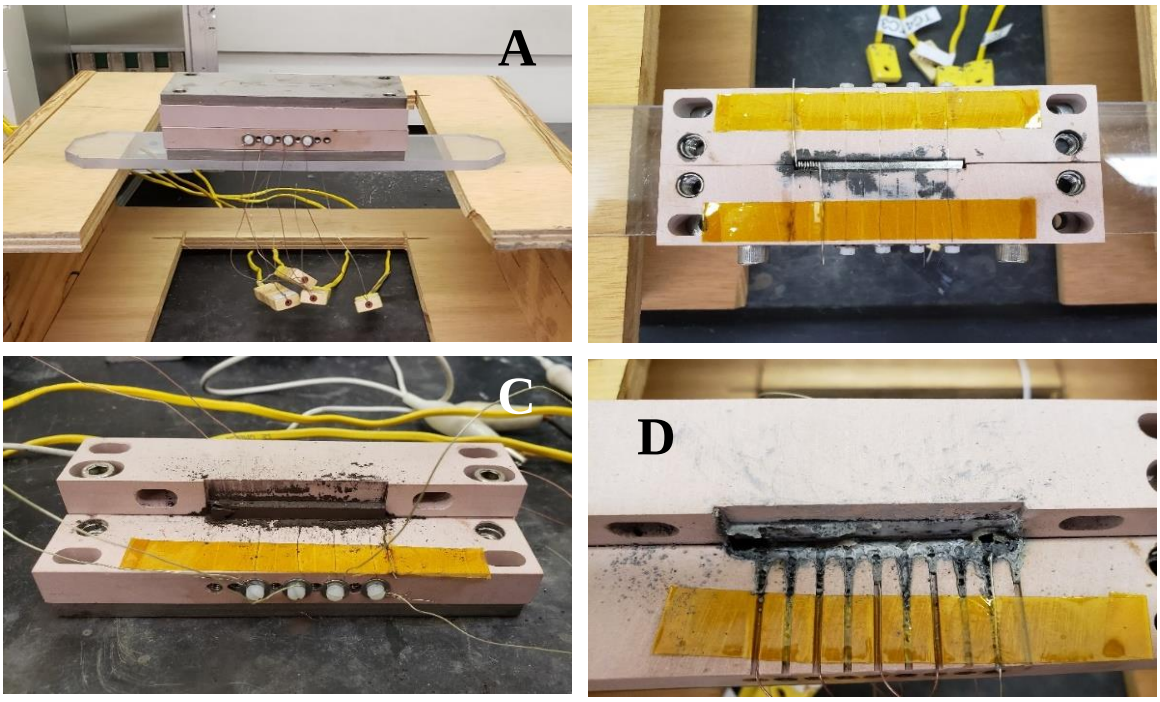

Figure 11: (A) The completely assembled ceramic propagation rate cell. (B) A view to the interior of the cell, showing thermocouples evenly spaced and coiled nichrome wire. (C) One of 4 ceramic blocks removed to show interior compressed pyrolant shape. (D) Post-reaction residue after successful ignition of pyrolant.

The graphite chamber is shown in Figures 12a-d. The interior rectangular chamber of this cell has identical dimentions to that of the ceramic cell in Figures 11a-d. Thermocouple channels machined in this cell are made slightly deeper and wider to accommodate thicker guage thermocouple wire if this is desired.

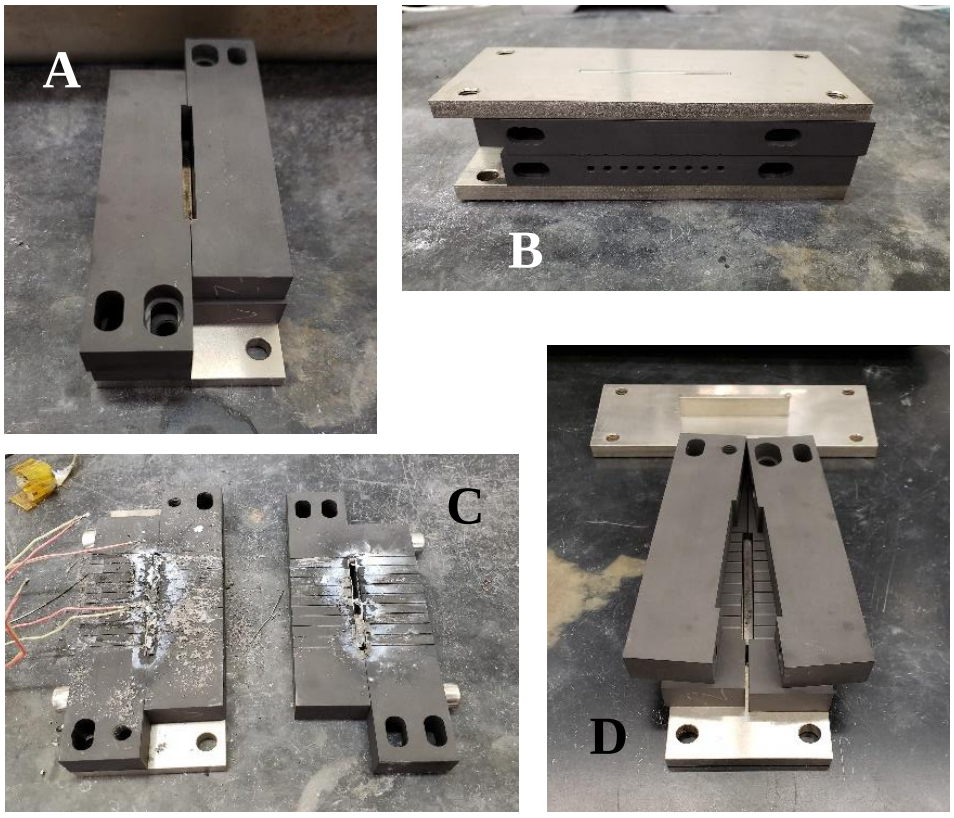

Figure 12: (A) The graphite propagation cell, showing the central test chamber formed from the blocks once they are assembled. (B) The completely assembled graphite propagation cell. (C) Burned pyrolant residue after a successful ignition. (D) View of graphite blocks nearly assembled. The stainless steel top and base contain a protruding slot which fits within the rectangular chamber to contain the pyrolant.

In order to control the atmosphere surrounding the burning pyrolant, a purge box was constructed to house the propagation cell (Figure 13). The box consists of an acrylic enclosure, each side of which is solvent welded at the edges. The box is placed on top of a table which holds the propagation cell and thermocouple ports, and is held tightly onto a gasket (orange) with 8 screws. A gas inlet is located at the bottom of the chamber, and an outlet is placed near the top of one side of the acrylic box which allows a continuous flow of gas to purge the environment of any

air (particularly oxygen). The thermocouple and ignition wires are threaded through a port in the bottom of the table which has been made gas-tight by filling with epoxy. Prior to pyrolant ignition, the box is purged with the desired gas for 15 minutes and gas continues to flow during ignition and burning.

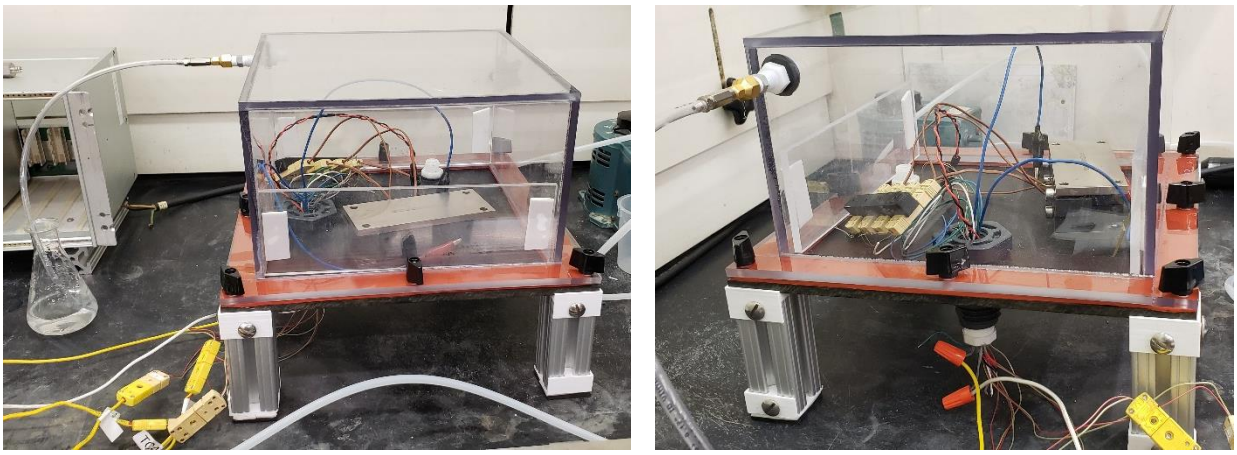

Figure 13: A purge box allows control of the environment surrounding the propagation cell. A continuous flow of gas enters and exits the box, purging of air before and during pyrolant ignition.

CHAPTER 4: RESULTS

4.1 Pyrolant Selection

Although the 18 pyrolant mixtures were chosen based on their high energy densities, it was initially unknown if each pyrolant would ignite via a nichrome wire, how explosively the pyrolants would react, or if any of the pyrolant reactions would incur harmful damage to the main propagation cell or its components. Pyrolants which failed to ignite via the nichrome wire test did not proceed to the next selection test, since they ultimatly would not combust within the propagation cell. Pyrolants which underwent large visual or audible detonations within the crucible were also not selected as immediately viable for propagation experiments. However, such excessively energetic pyrolant mixtures could become useful in the future as additives to slower-burning solid pyrolant reactions in order to speed up reaction propagation.

Groups of pyrolant mixtures which contained similar compounds reacted similarly to each other in the ignition and explosivity tests. The results for all tests are summarized in Table 7. Reactions between lithium peroxide and titanium diboride ($Li_2O_2 + TiB_2$; reaction #4) as well as aluminum and manganese dioxide ($Al + MnO_2$; reaction #10) were unable to be ignited via the nichrome wire method. Pyrolants containing magnesium (Mg), zirconium (Zr), and teflon (C_2F_4) exhibited loud cracking explosions often accompanied by visible flashes of light. Although the reaction between lithium peroxide and silicon ($Li_2O_2 + Si$; reaction #5) was not characterized as explosive, the reaction combusted rapidly.

Thermogravimetric analysis of the remaining pyrolants resulted in successful ignition and burning for the majority of samples. However, the reaction between titanium and boron (Ti + B; reaction #7) did not result in any ignition at temperatures up to 600 °C. Figure 14 shows the TGA results of all successful pyrolant mixtures containing lithium peroxide. The samples showed

insignificant mass loss up to 350 °C, and at approximately 350 °C, all samples exhibited a sharp decrease in mass. Between 400 – 450 °C samples show an inconsistent degree of mass gain, followed by a second decline in mass. The values of these changes are recorded in Table 6.

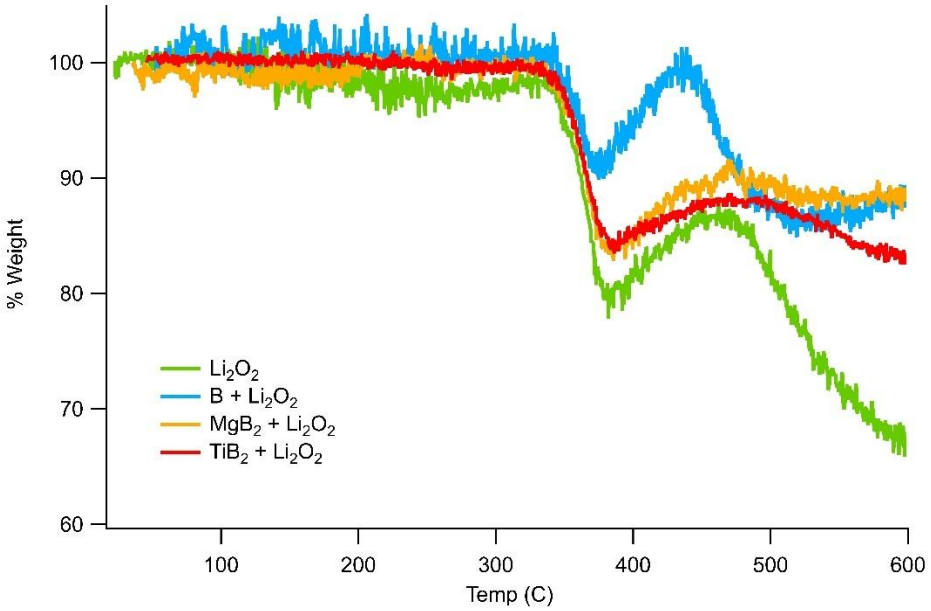

Figure 14: Thermogravimetric analysis (TGA) of pure lithium peroxide powder and 3 stoichiometric pyrolant reaction mixtures.

Table 6: Values of %weight at 350°C as well as sample masses at 600°C for each of the pyrolant samples in Figure 14.

Pyrolant Sample	$M_{350°C}$ (% weight)	$M_{600°C}$ (% weight)
Li_2O_2	81.1	67.2
$B + Li_2O_2$	90.5	87.2
$MgB_2 + Li_2O_2$	84.4	88.1
$TiB_2 + Li_2O_2$	84.8	82.7

Pyrolants which passed the ignition and explosivity test were subject to the graphite propagation test regardless of TGA test results. Experiments in this vertical propagation cell were meant to be analagous to the horizontally-lying propagation cells, and were designed to analyze the interactions between the pyrolant and thermocouples. For all pyrolants, burning of the powders resulted in one or more problematic interactions with the thermocouples. The burn products often

formed a hardened mass surrounding the thermocouple junction, melted the thermocouple junction altogether, or the hardened solid product replaced the thermocouple junction after it was melted, all of which can produce false temperature readings. Two examples of thermocouple noise are displayed in Figures 15a and b. Figure 15a is almost ideal, but peaks are closely spaced, indicating a fast propagation rate and thermocouples 3 and 4 (TC3, TC4) seem to experience noise between 1 and 2 seconds. Figure 15b shows temperature curves commonly seen for excessive electrical contact between the 4 thermocouples. Thermocouples 1, 3, and 4 show clear repetition in their peaks, which align with the peaks in neighboring thermocouples in multiple instances. Additionally, thermocouple 4 in Figure 15b also shows the signal produced when a complete breakage occurs in the thermocouple junction. This can be seen at about 9.5 seconds as the temperature curve shoots above the maximum range of a K-type thermocouple.

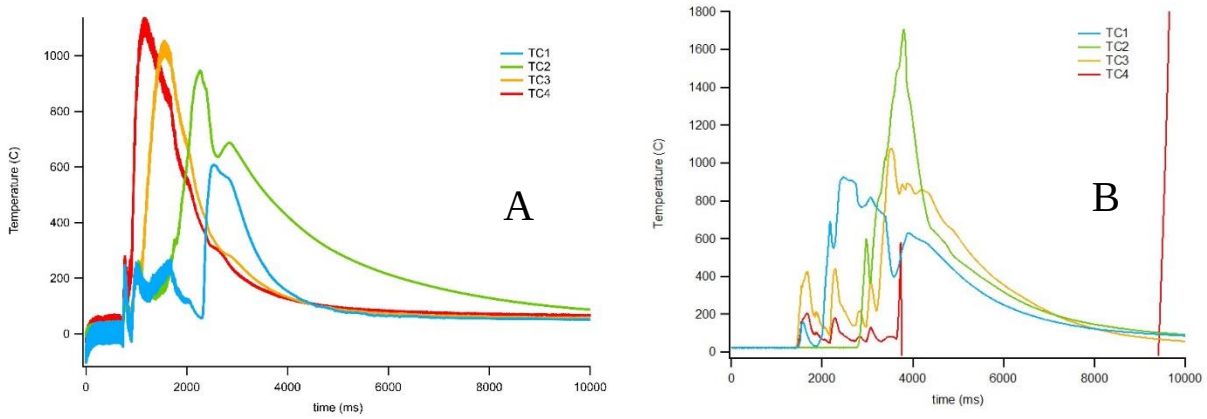

Figure 15: First vertical graphite cell reactions. (A) Reaction monitored with standard thermocouple wires. (B) Reaction monitored with one of the thermocouple wire pairs in electrical contact with the graphite cell.

Thus, of the 18 pyrolant reaction candidates assessed, mixtures with lithium peroxide and boron (Li_2O_2 + B; reaction #1), magnesium diboride (Li_2O_2+ MgB_2; reaction #2), as well as aluminum and molybdenum oxide (Al + MoO_3; reaction #11) were the leading candidates.

Reaction 11 was not chosen among the 3 due to its lower energy density as well as the availability of molybdenum oxide. Reaction 1 containing boron oxide was ultimately chosen due to the availability of boron powder.

Table 7: Results of the selection tests for each of the 18 pyrolants. A dash ("-") indicates the reaction did not proceed to that test.

#	Reaction	Nichrome Wire Test	TGA <600°C	Graphite Cell Test
Group 1: Lithium Peroxide				
1	$Li_2O_2 + B$	✓ Ignition (fizzle)	✓ Burn	TC breakage
2	$Li_2O_2 + MgB_2$	✓ Ignition (fizzle)	✓ Burn	TC breakage
3	$Li_2O_2 + Mg$	Ignition (explosive)	-	-
4	$Li_2O_2 + TiB_2$	No ignition	✓ Burn	-
5	$Li_2O_2 + Si$	Ignition (rapid, noiseless)	✓ Burn	-
6	$Li_2O_2 + Zr$	Ignition (explosive)	-	-
Group 2				
7	Ti + B	Ignition (explosive)	No Burn	-
8	Ti + C	*Postponed*	-	-
9	$Si + O_2(g)$	*Postponed*	-	-
10	$Al + MnO_2$	No ignition	-	-
11	$Al + MoO_3$	✓ Ignition (slow)	✓ Burn	TC breakage
Group 3: Magnesium and Teflon				
12	$Mg + Fe_2O_3$	Mg: too energetic	-	-
13	$Mg + Fe_3O_4$	Mg: too energetic	-	-
14	Mg + CuO	Mg: too energetic	-	-
15	$Mg + MnO_2$	Mg: too energetic	-	-
16	$Mg + Si + O_2(g)$	Mg: too energetic	-	-
17	$C_2F_4 + Mg$	C_2F_4: too energetic	-	-
18	$C_2F_4 + Li$	C_2F_4: too energetic	-	-

4.2 Thermocouple Noise Reduction

Prevention of thermocouple melting using a liquid polysilizane coating slightly reduced the occurances of complete breakage of the thermocouples. However, application of the coating was imperfect and prone to errors, since the polysilizane dried as a thick crust, which easily crumbled when the thermocouple junction was inserted into the pyrolant powder. As shown in Figure 16, the coating did not eliminate electical noise.

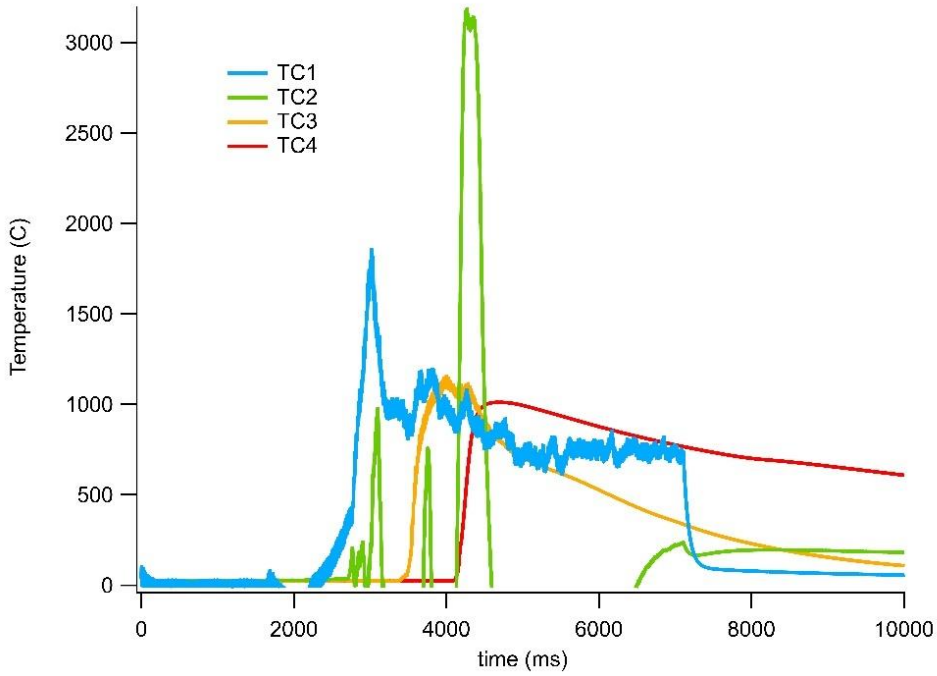

Figure 16: Vertical graphite cell reaction using polysilizane-coated thermocouples to prevent melting.

Coatings of boron nitride suffered less crumbling and remained on the thermocouple wires during insertion into the propagation cell. However, as shown in Figure 17, boron nitride seemed to provide little to no protection for electrical interferance.

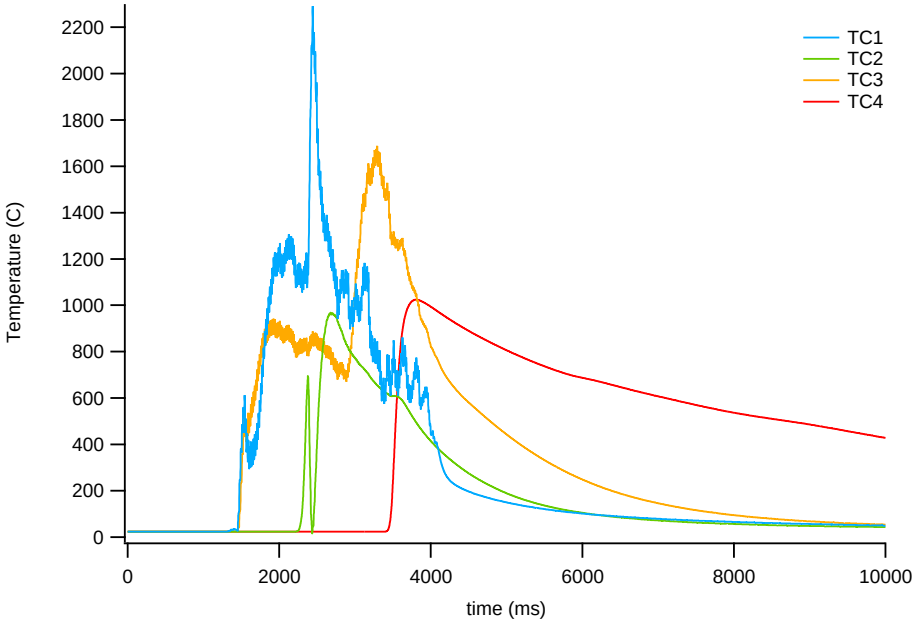

Figure 17: Vertical graphite cell reaction using boron nitride-coated thermocouples to prevent electrical interferance within the pyrolant powder.

CHAPTER 5: DISCUSSION

5.1 Lithium Peroxide + Boron Reaction Mechanism

It was determined via thermogravimetric analysis that the pyrolysis reaction between boron and lithium peroxide proceeds through 3 elementary steps, shown in Equations 5.1-5.3. Equation 5.4 shows the summation of these elementary steps to form the overall chemical equation. The first two elementary steps both involve the evolution or sequestration of a gas, which allowed us to elucidate those steps via TGA.

$$Li_2O_2\ (s) \rightarrow\ Li_2O\ (s) +\ O_2(g) \quad (5.1)$$

$$B\ (s) +\ O_2\ (g) \rightarrow\ B_2O_3\ (s) \quad (5.2)$$

$$Li_2O\ (s) +\ B_2O_3\ (s)\ \rightarrow\ Li_2B_4O_7(s) \quad (5.3)$$

$$\boldsymbol{Li_2O_2\ (s) +\ B\ (s) \rightarrow\ Li_2B_4O_7\ (s)} \quad (5.4)$$

The first elementary step in Equation 5.1 describes the decomposition of lithium peroxide to form lithium oxide and oxygen gas. This decomposition is observed at 350°C in all of our pyrolant samples containing Li_2O_2 in the form of a significant mass decrease. In the pure lithium peroxide sample in Figure 18, the decomposition results in a mass loss of 24.5wt%. These TGA results compare well to those in the literaure of lithium compounds which show a similar decline in mass for lithium peroxide at a temperature near 350°C (Figure 19) [30]. Assuming the reaction in Equation 5.1 goes to completion, the theoretical yield of lithium oxide (Li_2O) is 34.8 wt%, which is in agreement with the wt% value of Li_2O_2 observed in the literature. However, our lithium peroxide sample displayed in green in Figure 18 does not reach this theoretical value before a rapid mass increase occurs between 400-500°C. This indicates Li_2O_2 decomposition was incomplete before the formation of an unknown species, which seems to subsequently decompose between 450-500°C.

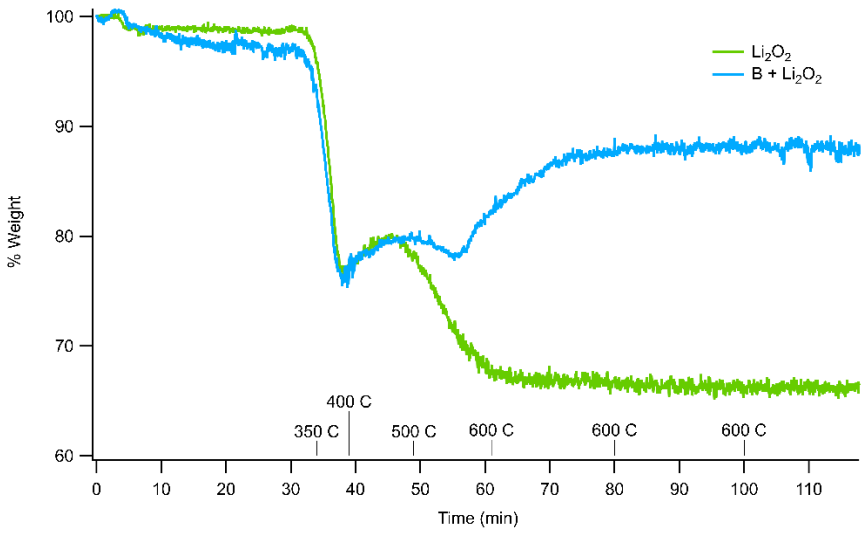

Figure 18: TGA of a pyrolant mixture containing Li_2O_2 (blue) as compared to a pure Li_2O_2 sample (green) shows the differences in behavior above 550°C as the pyrolant oxidizes leading to a mass increase, while pure Li_2O_2 does not.

The lithium peroxide curve eventually reaches 67.2 wt%; 65.2 wt% would indicate 100% decomposition. However, Figure 14 shows that the pyrolant mixtures do not plateau at a lower mass, as does the pure oxidant. An isothermal hold of our boron pyrolant mixture (blue curve) at 600°C (Figure 18) confirmed an increase in mass up to 88.3 wt%. This occurs as oxygen evolves from the first elementary step (Equation 5.1) and reacts with boron to form boron trioxide (Equation 5.2). We predict that a TGA run flowing air instead of argon gas over the sample would allow the pyrolant mixture B + Li_2O_2 to reach its maximum yield by supplying an excess amount of oxygen gas. Table 8 lists the final weight percent values for the curves in Figure 18 at temperatures 350°C and 600°C, as well as the theoretical wt% values given complete decomposition of Li_2O_2 at 350°C and complete oxidation of B at 600°C. We predict that the products Li_2O and B_2O_3 from the first two elementary reactions then react to produce lithium borate (Equation 5.3). Similarly, mixtures of lithium peroxide with magnesium diboride (MgB_2) and titanium diboride (TiB_2) should recover their mass in an extended isothermal run at 600°C in

the TGA with a flow of excess oxygen. In addition to B_2O_3 they should form the oxides MgO and TiO_2.

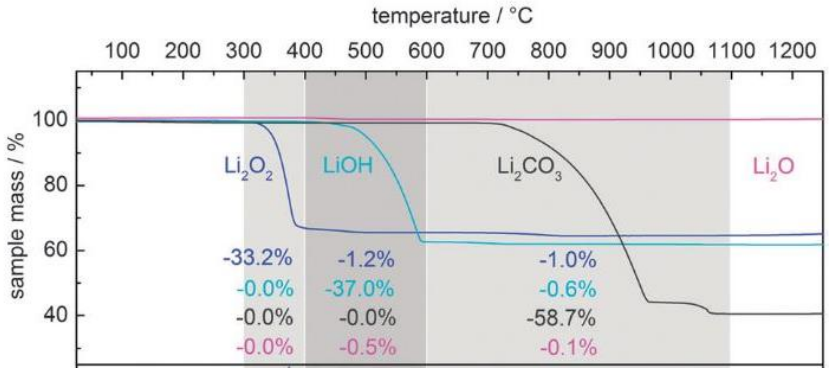

Figure 19: TGA results of lithium compounds held to temperatures of 1200°C. [30]

Table 8: TGA percent weight values of 4 samples at 2 different temperatures, as compared to their theoretical weight percents after the decomposition of lithium peroxide and after oxidation of the solid fuel. The decomposition of lithium peroxide should occur at 350°C.

Pyrolant Sample	$M_{350°C}$ (% wt)	$M_{350°C,\ theoretical}$ (% wt)	$M_{600°C}$ (% wt)	$M_{600°C,\ theoretical}$ (% wt)
Li_2O_2	75.5	65.2	67.2	65.2
B + Li_2O_2	75.7	69.9	88.3	100

5.2 Propagation of Lithium Peroxide + Boron Pyrolant

One ideal propagation reaction between lithium peroxide and boron is shown in Figure 20. The large temperature peaks in the graph mark each moment the combustion front passes a thermocouple as it proceeds along the length of pyrolant. In addition to Figure 20, the propagations shown in Figures 21-23 depict nearly ideal propagation results as compared to the problematic results shown in Figures 15b, 16, and 17. They each convey a significant noise reduction, no thermocouple breakage (with the exception of Figure 21), and minimal electrical interferance. However, temperature fluctuations can be caused by other phenomena, such as heat conduction

from the ignition wire, heat conduction eminating from the combustion front (preheating), phase changes, and electrical interferance.

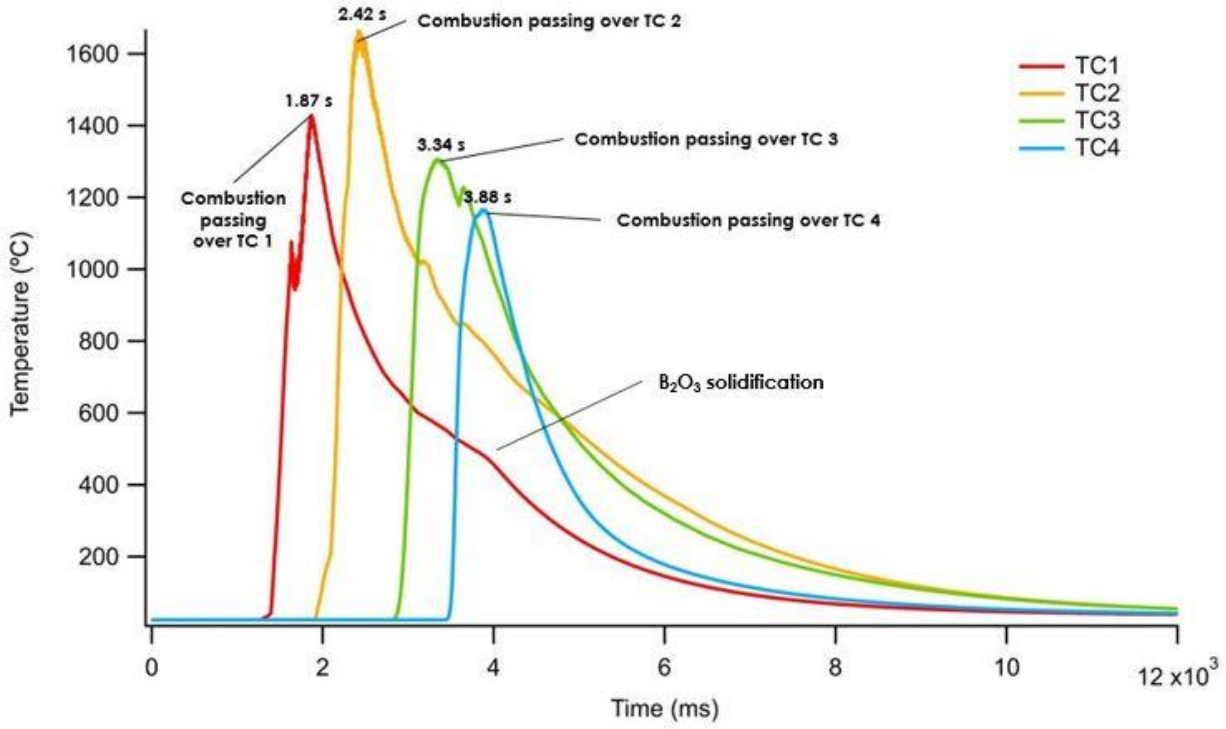

Figure 20: Reaction propagation for the reaction of lithium peroxide and boron using the graphite propagation cell and a nichrome wire.

5.2.1 Wire Heating

As current flows through the ignition wire, some heat generated may begin to conduct through the pyrolant regardless of whether the pyrolant has ignited. This may occur if the ignition wire is activated, the pyrolant rapidly ignites and causes the combustion front to pass quickly over the first few thermocouples, then heat directly from the ignition wire reaches the nearest thermocouple: likely thermocouple 1, causing a secondary spike in temperature.

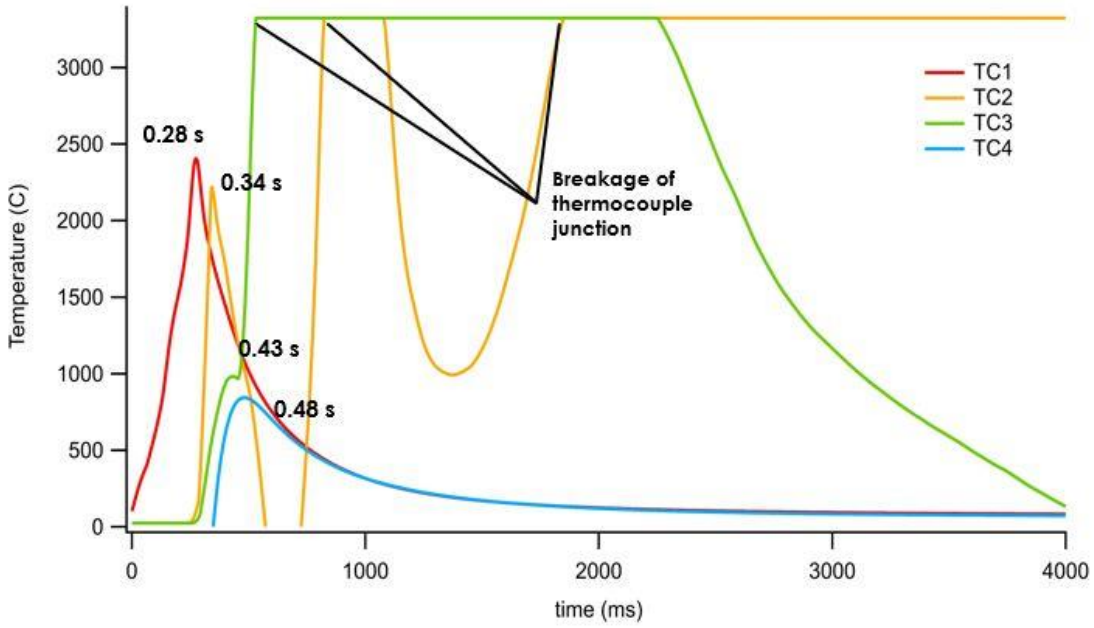

Figure 21: Reaction propagation for the reaction of lithium peroxide and boron using the graphite propagation cell and a tungsten wire. The flatlining of the thermocouples above 3000°C indicates a breakage of the thermocouple junction. This propagation occurred the most rapidly (combustion front passes over TC1 at <0.5s), and resulted in the fastest propagation rate.

5.2.2 Preheating

Heat conduction traveling forward from the point of burning pyrolant can cause preheating within the powder. Although similar to wire heating, the origin of the conduction is from the burning pyrolant itself rather than the ignition wire. Preheating causes downstream pyrolant to increase in temperature prior to it fully combusting. An example of this can be seen in TC2 of Figure 20 at t=2 ms, where there is a slight change in slope of the temperature curve at 200°C. Furthermore, this temperature fluctuation arises at a time between the combustion front leaving TC1 and reaching TC2. Moments after the preheating in the TC2 region, TC2 experiences the wave front of burning pyrolant.

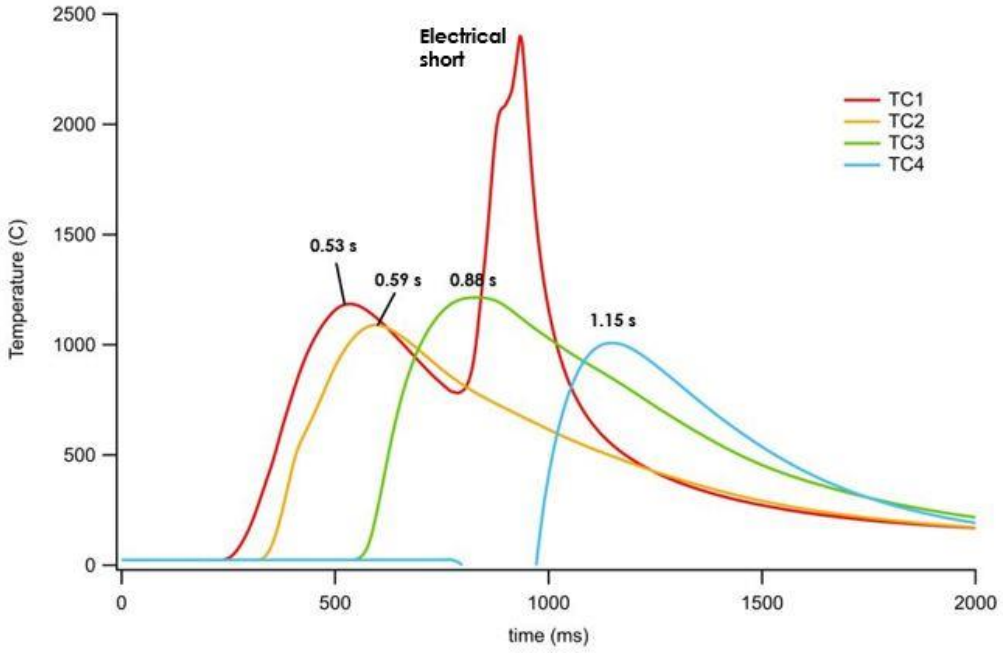

Figure 22: Reaction propagation for the reaction of lithium peroxide and boron using the graphite propagation cell and a tungsten wire. This reaction resulted in significant wire heating, as observed in TC1. This propagation bears strong resemblance to the propagation shown in Figure 23, a promising result for achieving reproducability.

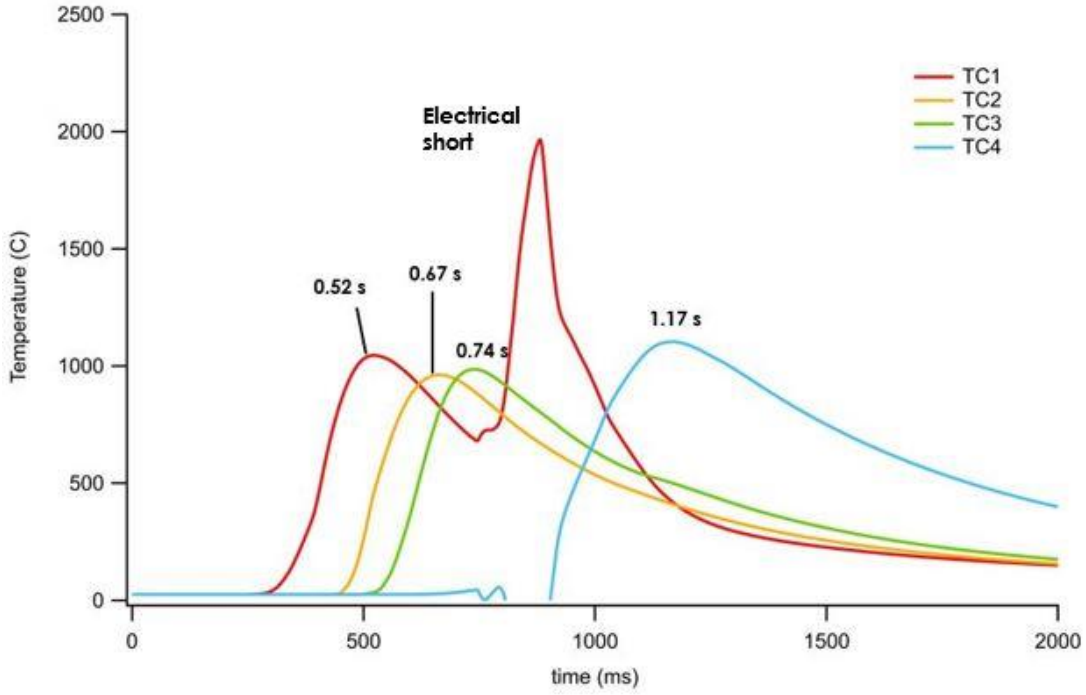

Figure 23: Reaction propagation for the reaction of lithium peroxide and boron using the graphite propagation cell and a tungsten wire. This reaction resulted in significant wire heating, as observed in TC1. This propagation bears strong resemblance to the propagation shown in Figure 22, a promising result for achieving reproducability.

5.2.3 Phase Change

As discussed in section 1.2, heat can be absorbed by our products during melting or vaporization, and heat can be released via solidification or condensation. The melting and boiling points of the intermediate and overall products of the reaction between boron and lithium peroxide are listed in Table 9. The relatively low melting point of boron trioxide (B_2O_3) allows its phase change to be seen in some of our propagation curves, notably in Figures 20 and 24.

Table 9: The melting and boiling points for anticipated reaction products. *The boiling point of $Li_2B_4O_7$ was estimated from $Na_2B_4O_7$.

Product	Melting Point (°C)	Ref.	Boiling Point (°C)	Ref.
Li_2O	1843	[29]	-	-
B_2O_3	450	[31]	1860	[32]
$Li_2B_4O_7$	1190	[29]	1873	*

5.2.4 Electrical Interferance

An extreme example of electrical interferance was shown in Figure 15b. Due to the nature of our experimental set up, our 4 thermocouples should experience a rise in temperature in chronological order. There should be little cause for peaks to be mirrored in multiple thermocouples at the same instant in time. Figure 15b shows various instances where thermocouples 1, 3, and 4 are all experiencing simultaneous temperature peaks. Unlike other temperature peaks, these fluctuations are caused by stray electrons. Since the reaction between boron and lithium peroxide is a reduction-oxidation (redox) reaction, electrons migrating within the pyrolant can be inadvertently channeled through the thermocouple wires, producing electrical interference that can behave like a temperature increase. Due to the electrical conductivity of the graphite cell, electrons entering the graphite can then migrate to neighboring thermocouples. In a case of mild interferance these perturbations can be identified by looking for “bumps” in a

temperature curve that occur at the same time as the burning wave front in another thermocouple. In Figure 20 for example, TC2 exhibits a slight temperature increase at the same time that the burning passes TC3 and TC4.

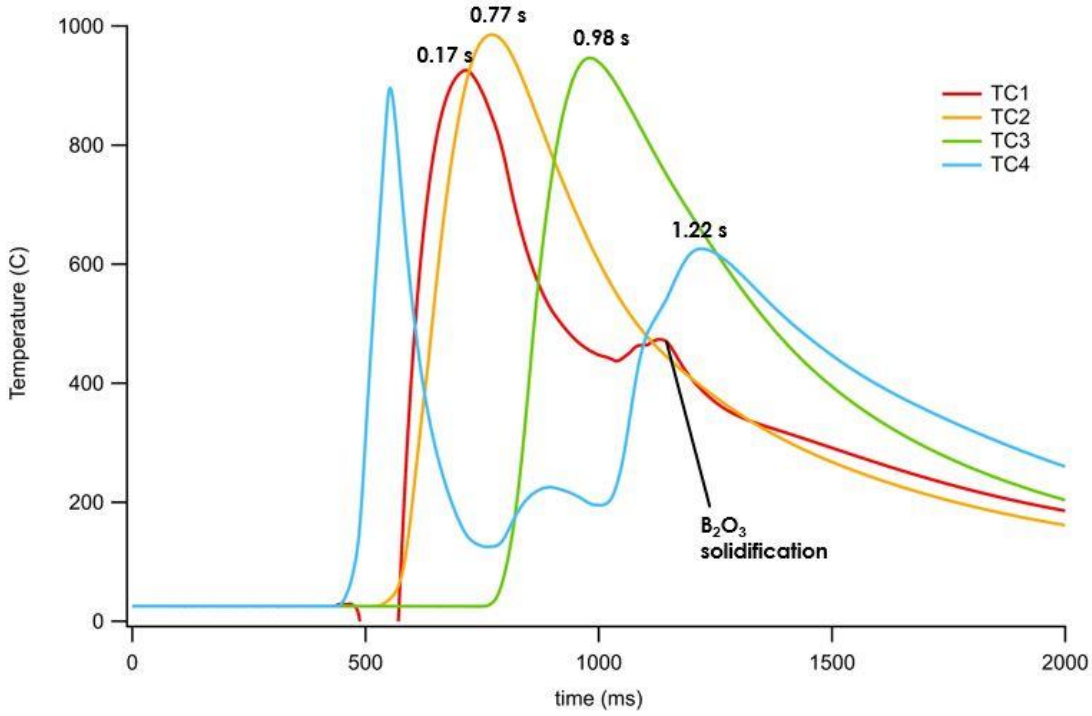

Figure 24: Reaction propagation for the reaction of lithium peroxide and boron using the graphite propagation cell and a tungsten wire. The phase change of boron oxide from liquid to solid is visible in TC1 as that region cools.

5.2.5 Rate Calculations

A rate calculation can be made by determining the times the temperature spikes occur since the distances between each thermocouple is known to be 1 cm. The overall rate calculation between the first and last thermocouple is shown in Equation 5.5, where x is the location of a thermocouple and t is the time at which the combustion front passes over a thermocouple.

$$v_{propagation} = \frac{\Delta x_{TC}}{\Delta t_{TC}} = \frac{x_{TC4} - x_{TC1}}{t_{TC4} - t_{TC1}} \tag{5.5}$$

The overall reaction propagation for the experimental run shown in Figure 20 was 1.49 cm/s, which has been our slowest (and therefore best) achieved propagation rate. The rates for many other propagation reactions discussed are listed in Table 10. A singular reaction was performed under nitrogen atmosphere by using N_2 as the purge gas (Figure 21). The utilization of nitrogen resulted in the fastest observed propagation rate of 14.49 cm/s. The highest reaction temperatures achieved in our graphite cell seem to fall within a wide range from 600 – 1400°C. In addition, reaction rates can be inconsistent between thermocouples within the same pyrolant reaction. For example, a peak from TC3 can be closer to TC2 than it is to TC4, indicating the reaction rate increased in the central region of the pyrolant. Inadvertant differences in the packing density of the pyrolant powder within the cell could be a likely cause of these rate changes. A higher packing density in a region of our rectangular chamber could cause a decrease in the propagation rate, since less oxygen permeates the powder and more powder is available for burning.

Table 10: The propagation rates of lithium peroxide and boron pyrolant reactions run with different cell parameters.

#	Cell Type	Wire Type	Atmosphere	Propagation rate (cm/s)	Figure #
1	Graphite	Nichrome	Air (high exposure)	2.21	15a
2	Graphite	Nichrome	Air (tightly sealed)	1.49	20
3	Graphite	Tungsten	Nitrogen	14.49	21
4	Graphite	Tungsten	Argon	4.89	22
5	Graphite	Tungsten	Argon	4.63	23
6	Graphite	Tungsten	Argon	5.92	24

CHAPTER 6: CONCLUSION

In this research study, a number of solid exothermic reactions were selected as potential pyrolants with a range of energy densities between 0.8 – 9.0 kWh/kg. These pyrolants were evaluated for use as fuels for long-duration space missions. Ultimately, of 18 pyrolants, the reaction between lithium peroxide (Li_2O_2) and boron (B) was chosen as the initial fuel candidate. The mechanism of the reaction was determined to proceed through 3 elementary steps: a) the decomposition of lithium peroxide (Li_2O_2) to form lithium oxide (Li_2O), b) the oxidation of boron (B) to form boron oxide (B_2O_3), and c) the reaction of the solid products to form lithium tetraborate ($Li_2B_4O_7$). A slow propagation rate of 1.49 cm/s was achieved by this reaction without the need of any solid additives or external control to further slow burning. This indicates that addition of solid additives with high heat capacity or low melting points could slow the reaction even further and provide a prolonged heat release. Thus, the exothermic reaction between Li_2O_2 and B is a promising candidate for the generation and harvesting of heat to be used as an energy source.

LIST OF REFERENCES

[1] Launius, R. D., 2004, Frontiers of space exploration, Greenwood Publishing Group.

[2] O'Donnell, D. J., 1994, "Overcoming barriers to space travel," Space Policy, 10(4), pp. 252-255.

[3] Vedda, J., 2008, "Challenges to the Sustainability of Space Exploration," Astropolitics, 6, pp. 22-49.

[4] Masson-Zwaan, T., and Freeland, S., 2010, "Between heaven and earth: The legal challenges of human space travel," Acta Astronautica, 66(11), pp. 1597-1607.

[5] Iliopoulos, N., and Esteban, M., 2020, "Sustainable space exploration and its relevance to the privatization of space ventures," Acta Astronautica, 167, pp. 85-92.

[6] 2016, "Space Travel: Risk, Ethics, and Governance in Commercial Human Spaceflight," New Space, 4(2), pp. 83-97.

[7] Bainbridge, W. S., 2009, "Motivations for space exploration," Futures, 41(8), pp. 514-522.

[8] Braddock, M., 2017, "Ergonomic challenges for astronauts during space travel and the need for space medicine," J Ergonomics, 7(221), p. 2.

[9] Genah, S., Monici, M., and Morbidelli, L., 2021, "The Effect of Space Travel on Bone Metabolism: Considerations on Today's Major Challenges and Advances in Pharmacology," International Journal of Molecular Sciences, 22(9), p. 4585.

[10] Galts, C., 2017, "A journey to Mars: The medical challenges associated with deep space travel and possible solutions," University of British Columbia Medical Journal, 8, pp. 38-39.

[11] Euroconsult, 2018, "Government Funding in Space Exploration to Surpass $20 Billion by 2027," Prospects for Space Exploration

[12] Dunbar, B., 2021, "Planetary Missions Program Office," https://www.nasa.gov/planetarymissions/overview.html.

[13] Martinez-Sanchez, M., and Pollard, J. E., 1998, "Spacecraft Electric Propulsion-An Overview," Journal of Propulsion and Power, 14(5), pp. 688-699.

[14] Bathgate, S. N., Bilek, M. M. M., and McKenzie, D. R., 2017, "Electrodeless plasma thrusters for spacecraft: a review," Plasma Science and Technology, 19(8), p. 083001.

[15] Shubov, M., 2021, "Gas Core Reactors for Deep Space Propulsion," arXiv preprint arXiv:2105.11533.

[16] Bermudez-Garcia, A., Voarino, P., and Raccurt, O., 2021, "Environments, needs and opportunities for future space photovoltaic power generation: A review," Applied Energy, 290, p. 116757.

[17] Levchenko, I., Xu, S., Teel, G., Mariotti, D., Walker, M., and Keidar, M., 2018, "Recent progress and perspectives of space electric propulsion systems based on smart nanomaterials," Nature communications, 9(1), pp. 1-19.

[18] David W. Miller, J. K., 2003, "Spacecraft Power Systems," Massachusetts Institute of Technology, OpenCourseWare.

[19] Pu, Z., Zhang, G., Hassanpour, A., Zheng, D., Wang, S., Liao, S., Chen, Z., and Sun, S., 2021, "Regenerative fuel cells: Recent progress, challenges, perspectives and their applications for space energy system," Applied Energy, 283, p. 116376.

[20] Dunbar, B., 2021, "Watts on the Moon Challenge," nasa.gov/wattson.

[21] Dunbar, B., 2017, "Juno Spacecraft and Instruments," https://www.nasa.gov/mission_pages/juno/spacecraft/index.html.

[22] Thompson, J. R., "Meet Europa Clipper," https://europa.nasa.gov/spacecraft/meet-europa-clipper/.

[23] 2021, "Electrical Power," https://mars.nasa.gov/mars2020/spacecraft/rover/electrical-power/.

[24] Chahal, M. S., 2012, "European Space Nuclear Power Programme: UK Activities," UK Space Agency.

[25] Barnett, A., "In Depth: Ulysses," https://solarsystem.nasa.gov/missions/ulysses/in-depth/.

[26] Piazza, E., "Legacy Power Systems," https://rps.nasa.gov/power-and-thermal-systems/legacy-power-systems/.

[27] Steven D. Howe, T. R., Douglas Crawford, Jorge Navarro, 2013, "Economical Production of Pu-238," Nuclear and Emerging Technologies for Space Albuquerque, NM.

[28] Peter Atkins, J. d. P., 2010, Physical Chemistry, Oxford University Press, Great Britain.

[29] Technology, N. I. o. S. a., 2018, "NIST Chemistry WebBook," U.S. Department of Commerce.

[30] Nefedov, R. A., Ferapontov, Y. A., and Kozlova, N. P., 2016, "Problem of the lithium peroxide thermal stability," IOP Conference Series: Materials Science and Engineering, 112, p. 012027.

[31] Health, T. N. I. f. O. S. a., 2019, "NIOSH Pocket Guide to Chemical Hazards," Centers for Disease Control and Prevention (CDC).

[32] Cole, S. S., and Taylor, N. W., 1935, "THE SYSTEM Na2O-B2O3, IV Vapor Pressures of Boric Oxide, Sodium Metaborate, and Sodium Diborate between 1150°C and 1400°C," Journal of the American Ceramic Society, 18(1-12), pp. 82-85.